

Article

Reducing Aerodynamic Drag on Roof-Mounted Lightbars for Emergency Vehicles

Michael Gerard Connolly ^{*}, Malachy J. O'Rourke  and Alojz Ivankovic 

School of Mechanical and Materials Engineering, University College Dublin, Dublin 4, D04 PR94 Dublin, Ireland; malachy.orourke@ucd.ie (M.J.O.); alojz.ivankovic@ucd.ie (A.I.)

* Correspondence: michael.connolly@ucdconnect.ie

Abstract: This paper investigates the impact of contemporary lightbars on vehicle fuel efficiency with a focus on quantifying their effects on fuel consumption and exploring strategies to improve drag performance through modifications. Simulations showed an 8–11% increase in drag for square-back vehicles, with greater penalties outlined for vehicles with rear-slanting roofs. Given the moderate drag increase, the impact on the driving range, especially for electric vehicles, remains minimal, supporting the continued use of external lightbars. Positioning experiments suggest marginal drag reductions when lowering the lightbar to its lowest position due to additional drag effects that can be caused by the mounting mechanism in its condensed form. Angling the lightbar showed negligible drag increases up to an angle of 2.5 degrees, but beyond that, a 4% increase in drag was observed for every additional 2.5 degrees. Additionally, fitting drag-reducing ramps ahead of the lightbar yielded no significant drag savings. Noise analysis identified that the lightbar's wake and rear surfaces were responsible for the largest production of noise. The optimal lightbar design was found to incorporate overflow rather than underflow and rear tapering in sync with roof curvature. Appendable clip-on devices for the lightbar, particularly rear clip-ons, demonstrated appreciable drag reductions of up to 2.5%. A final optimised lightbar design produced a minimal 2.8% drag increase when fitted onto an unmarked vehicle, representing a threefold improvement compared with the current generation of lightbars. This study advances the field of lightbar aerodynamics by precisely quantifying drag effects by using highly detailed geometry and examines the significance of optimal positioning, angle adjustment, and appendable clip-on devices in greater depth than any existing published work.



Citation: Connolly, M.G.; O'Rourke, M.J.; Ivankovic, A. Reducing Aerodynamic Drag on Roof-Mounted Lightbars for Emergency Vehicles. *Fluids* **2024**, *9*, 113. <https://doi.org/10.3390/fluids9050113>

Academic Editors: Ivette Rodríguez and Benedetto Mele

Received: 5 April 2024
Revised: 24 April 2024
Accepted: 7 May 2024
Published: 11 May 2024



Copyright: © 2024 by the authors. Licensee MDPI, Basel, Switzerland. This article is an open access article distributed under the terms and conditions of the Creative Commons Attribution (CC BY) license (<https://creativecommons.org/licenses/by/4.0/>).

Keywords: drag reduction; CFD; lightbars; appendable devices; fuel savings

1. Introduction

With a global effort underway to reduce the greenhouse gas (GHG) emissions associated with transport, it is essential that all transport sectors consider ways to reduce the fuel and energy consumption of their road vehicles. The EEA estimates that around 25% of total GHG emissions come from transport [1]. One sector very suited for improvement is that of emergency vehicles, which is a broad group of road vehicles mainly consisting of police, ambulance, and fire department transports. Emergency vehicles require the use of lighting systems to announce their presence while helping clear a right away for their passage. Historically, these lighting systems consisted of large roof-mounted structures which used rotating incandescent beacons to produce light, which also produced large amounts of unwanted aerodynamic noise and drag. Today, lightbars have become much smaller to tackle these negative effects and mostly consist of low-profile, roof-mounted LED units, especially in the US and many EU countries. Internal lighting is also a popular option where lighting strips are fitted inside the front and rear windshields, which eliminates the drag production associated with the lightbar. A key disadvantage of these systems is that they do not provide 360-degree illumination, but they have the advantage of being suited for stealthier operations, similarly to low-profile lightbars. Different needs exist for

different departments, but when a vehicle operates outside an urban environment at high average speeds, the aerodynamic needs begin to outweigh visibility issues in the context of fuel expenditure and environmental impact.

The current challenge for fleet managers in these emergency departments is which option is best. With a push for increased electrification of fleets, the question of how much driving range is lost from the use of an external lightbar along with the additional CO₂ production and fuel usage needs to be answered. This article is aimed at answering these questions and looks to provide fleet managers with the metrics to best help them decide if the traditional roof-mounted lightbar is suitable for their electric vehicles. Additionally, the installers of these lightbar systems have questions on where best to install these lightbars and how best to position them on roofs for optimal drag and noise performance. The manufacturers of these lightbar systems are also key stakeholders and need to know what is the most optimal lightbar profile for drag reduction, as the majority of profiles in use today consist of generic high-aspect-ratio rectangles. Roof-mounted lightbars are generally fitted at the B pillars of a vehicle, as a structural support runs across the roof at this point, which is ideal for bolting the lightbar to the roof. Other methods for mounting include magnet mounts, which are less suitable for high-speed-chase scenarios where aerodynamic forces are high due to the risk of detachment. An additional consideration when incorporating a roof-mounted lightbar on a vehicle is handling, and how the presence of the lightbar affects the lift properties of the vehicle, which can be particularly important at high speed when cornering or overtaking. The importance of noise cannot be overstated. One instance described by a fleet manager for the Irish police force highlighted the issue of noise levels inside the cabin when vehicles are travelling at chase speeds. If a lightbar is not designed with noise reduction in mind, it can create a difficult working environment for officers. This was evident when a previous-generation lightbar was installed on a new fleet of Audi Q7s, which led to a temporary grounding of the fleet until modifications were made to reduce the noise levels inside the cabin at high speed.

2. Literature Review

The topic of lightbar aerodynamics has been studied for many decades; however, there is a noticeable lack of published academic articles on the topic. In the 1980s, several relevant articles were published in the US and Canada. A study conducted by the Illinois Department of Law Enforcement [2] estimated that USD 237,000 a year could be saved if the roof-mounted equipment on 1000 Marked vehicles were removed based on 1982 fuel prices. Improved top speed and acceleration were outlined as added benefits for the removal. Ref. [3] studied the effects of replacing roof-mounted lightbars with internal lightbars in the context of fuel consumption and accident rates. The article referenced a 1982 study that found that vehicles without roof lightbars had 6.4% better fuel economy. A new study on 208 vehicles found a 6.9% improvement in fuel economy for unmarked vehicles using internal lighting. Vehicles without roof-mounted lightbars were found less likely to be in accidents. Ref. [4] provided results from fuel consumption testing on three different police vehicles using six different lightbar designs. The best-performing lightbar increased fuel consumption by only 6.6%, while the worst increased it by 11.3%. The average was 8.5%. The study found much greater fuel efficiency for lower-profile lightbars. Choosing the lowest-drag lightbar was estimated to save the department USD 500,000 over 10 years. A 25% scale wind tunnel test [5] on a detailed notchback saloon found that when fitted with a generic lightbar, a 15.6% wind-averaged drag increase was observed. Notchback vehicles are particularly prone to high drag increases when fitted with roof equipment, as flow detachment in the wake of the equipment can generate considerable amounts of drag on the rear glass. A 2017 CFD study [6] showed that a 34% drag increase was realisable when adding a generic police siren to a BMW 5-series. The same authors conducted a study [7] into the effects of lightbars attached to the front and rear of a police van's roof, reporting a 32% drag increase. In both studies, the drag increases were considerably reduced by using streamlining techniques for the roof add-ons. In a previous study conducted in

2020 [8], three detailed vehicle configurations (notchback, small SUV, and large SUV) were fitted with a lightbar at three different locations along their roofs (A, B, and C pillars). The notchback vehicle reported the highest drag increase for all positions. Most notably, this was that due to the straight roofs of two SUV configurations, with the drag increases for both the B and C pillar positions being the same. On the small SUV, a lightbar mounted at the B pillar reported an 8.8% drag increase. Other studies that looked at similar roof mountings other than lightbars include [9], where methods to reduce drag on a protrusive taxi sign were discussed, such as orientation changes and drag-reducing ramps ahead of the sign. Similarly, a 2016 study [10] estimated that approximately 1% of total light-duty-vehicle fuel consumption in the US is attributable to roof racks. Lastly, a comprehensive review in 2016 [11] by the Joint Research Council for the European Commission outlined how the degree to which drag-increasing add-ons like roof racks and roof boxes increase fuel consumption is dependent on the vehicle’s shape. The article further addressed the need for more published material on the fuel consumption effects of vehicle add-ons to help estimate total fuel consumption for passenger vehicles. Excluding the articles referenced, there is very little else available in the literature to quantify the effects of external lightbars on emergency service vehicles, especially given all the global stakeholders that can benefit from research into reducing their associated negative effects on aerodynamics. This article looks to fill this gap by outlining an extensive study into the effects of lightbars fitted onto police vehicles in Ireland. Methods to reduce drag are discussed in detail, and in-depth quantification is provided for what the increased fuel consumption and range detriment will be when mounting standard lightbars for a wide range of police vehicles.

3. Computational Setup and Numerical Methodology

3.1. Governing Equations

The modelling of airflow over ground vehicles can be effectively accomplished through a continuum approach, focusing solely on macroscopic interactions. In this context, each fluid element represents the average behaviour of numerous fluid particles across both space and time. Air was modelled as an isothermal Newtonian fluid with constant viscosity and density. The constant density assumption was justified as the investigated flows had Mach numbers below 0.3, minimising compressibility effects. The governing equations that form the basis for CFD simulations are the Navier–Stokes equations (Equations (1) and (2)), which are derived from the principles of mass and momentum conservation. For steady incompressible flow, the transient term goes to zero in Equations (1) and (2). The body force term f_i is also set to zero. In Equations (1)–(5), u_i is the velocity component in the x_i direction, ρ is the fluid density, P is pressure, t is time, and μ is viscosity.

$$\frac{\partial \rho}{\partial t} + \frac{\partial(\rho u_i)}{\partial x_i} = 0 \tag{1}$$

$$\rho \frac{\partial u_i}{\partial t} + \rho \frac{\partial(u_i u_j)}{\partial x_j} = -\frac{\partial P}{\partial x_i} + \frac{\partial \tau_{ij}}{\partial x_i} + \rho f_i \tag{2}$$

$$\tau_{ij} = 2\mu S_{ij} - 2\mu S_{kk}\delta_{ij} \quad S_{ij} = \frac{1}{2} \left(\frac{\partial u_i}{\partial x_j} + \frac{\partial u_j}{\partial x_i} \right) \quad S_{kk} = \frac{1}{2} \left(\frac{\partial u_i}{\partial x_i} \right)$$

These two equations are then decomposed into fluctuating and mean components, as per Equation (3), to obtain the Reynolds Averaged Navier–Stokes (RANS) equations [12]. The CFD results detailed throughout this article were realised by using ANSYS Fluent, which solves the Reynolds Averaged Navier–Stokes (RANS) equations detailed below in Equations (4) and (5) with the help of turbulence models such as the $k - \omega$ SST model [13]. k is the turbulent kinetic energy, and ω is the specific rate of dissipation in this two-equation turbulence model.

$$u(t) = \bar{u}(t) + u'(t) \tag{3}$$

$$\frac{\partial \bar{u}_i}{\partial x_i} = 0 \tag{4}$$

$$\rho \frac{\partial \overline{u_i u_j}}{\partial x_j} = -\frac{\partial P}{\partial x_i} + \frac{\partial}{\partial x_j} \left(\mu \frac{\partial \bar{u}_i}{\partial x_j} - \overline{\rho u_i' u_j'} \right) \tag{5}$$

While RANS simulations are still an industry standard for aerodynamic simulations of ground vehicles in a time-efficient manner, hybrid large eddy simulations (LESs) are becoming increasingly popular due to advancements in computing power and the improved correlations seen between their results and wind tunnel data. Hybrid LES works by applying a RANS formulation in the boundary layer and then applying the LES formulation outside in the mixing layer and in regions where the flow is detached from the vehicle. Where a high number of configurations/runs are required, the computational expense associated with an entirely hybrid LES approach becomes too high, as each simulation can require more than 10 times the computational time required for a RANS simulation [14,15], as was the case for this study. Therefore, hybrid LES can be used as a verification method for a large number of RANS simulations by simulating only a short number of runs using hybrid LES and comparing the results against their corresponding RANS equivalents. One of the best hybrid-LES approaches available is Stress-Blended Eddy Simulation (SBES), which is a proprietary model by ANSYS. The model works by blending the turbulence stress tensor according to Equation (6) [16]. Here, the underlying RANS and LES models are unaffected, and in principle, any two models can be combined. If both models are based on eddy viscosity concepts, the formulation can be simplified as shown in Equation (7) [16]. The f_{SBES} shielding function is where the main complexity of the model exists, and details on how it works are undisclosed by ANSYS. The main advantage of SBES over other methods is its ability to rapidly transition between RANS and LES, giving rise to clearly distinguishable RANS and LES regions [16].

$$\tau_{ij}^{SBES} = \tau_{ij}^{RANS} f_{SBES} + \tau_{ij}^{LES} (1 - f_{SBES}) \tag{6}$$

$$\nu_{ij}^{SBES} = \nu_{ij}^{RANS} f_{SBES} + \nu_{ij}^{LES} (1 - f_{SBES}) \tag{7}$$

Aerodynamic noise generation related to road vehicles results from three different noise generation mechanisms. Mass flows through leaks and small openings (monopoles), impulses on surfaces due to pressure fluctuations (dipoles), and from turbulent free flows such as in the wake of a vehicle (quadrupole). Dipoles are the main source of noise in road vehicles, as quadrupole sources have low noise emission and monopole sources are eliminated for well-sealed vehicles [17]. Note that the acoustic power of a dipole grows with the sixth power of its speed [17]. This is particularly important for add-on parts that cause the flow to speed up, for example, as the flow passes underneath a lightbar or around a wing mirror. Predicting far-field noise requires a transient simulation, which has the underlying need for a hybrid-LES approach, to provide reliable predictions of flow fluctuations, which can be used to predict sound emission from sources such as vehicle panel work, which can then be received in the far field with a designated receiver.

The equations underpinning aeroacoustics start from Lighthill’s aeroacoustic analogy [18], in which a wave equation is derived from the compressible Navier–Stokes equations. This can be seen in Equation (8), where the right-hand side represents the source terms. Equation (9) is known as the Lighthill stress tensor, which has been approximated for the conditions of a low Mach number and High Re such that viscous effects and density fluctuations can be neglected. Additionally, isentropic and constant density flow is assumed.

$$\frac{\partial^2}{\partial t^2} (\rho - \rho_0) - c^2 \frac{\partial^2}{\partial x_i \partial x_j} (\rho - \rho_0) = \frac{\partial^2 T_{ij}}{\partial x_i \partial x_j} \tag{8}$$

$$T_{ij} = \rho_0 u_i u_j \tag{9}$$

Following on from this, the Ffowcs Williams and Hawkings model [19] was developed and can be used for the prediction of far-field noise. The equation behind the model is shown in Equation (10). The function $f = 0$ defines the mathematical surface enclosing all sources outside of which ($f > 0$) the solution is desired. V_i represents the velocities of surface f , $\delta(f)$ is the Dirac function, $H(f)$ is the Heaviside function, and c is the far-field sound speed. The right side represents the sources, with the first being the quadrupole, the second being the dipole, and the last term being the monopole. Equations (11) and (12) outline the formulation for F and Q in the dipole and monopole terms, respectively.

$$\frac{\partial^2 \rho}{\partial t^2} - c^2 \nabla^2(\rho) = \frac{\partial^2}{\partial x_i \partial x_j} \{T_{ij} H(f)\} + \frac{\partial F_i \delta(f)}{\partial x_i} + \frac{\partial Q_i \delta(f)}{\partial t} \quad (10)$$

$$F_i = -[\rho u_i (u_j - V_j) + p \delta_{ij} - \tau_{ij}] \frac{\partial f}{\partial x_i} \quad (11)$$

$$Q = [\rho (u_i - V_i) + \rho_0 V_i] \frac{\partial f}{\partial x_i} \quad (12)$$

Force measurements for the simulated geometry are produced in Fluent once the pressure is calculated at each cell in the vicinity of the geometry. It is common practice when designing and comparing vehicles to express the forces and moments on a vehicle in terms of dimensionless coefficients. The formulas for the two main force coefficients used throughout this article are detailed in Equations (13) and (14). C_D and C_L are the drag and lift coefficients, respectively. “ V ” is the free-stream velocity, while F_D and F_L are the drag and lift forces, respectively, which are computed from the CFD simulations. The “ A ” term in the formulas represents the projected frontal area of the vehicle. Note that a 0.001 C_D change is referred to as a 1 drag count change.

$$C_D = \frac{F_D}{\frac{1}{2} \rho V^2 A} \quad (13)$$

$$C_L = \frac{F_L}{\frac{1}{2} \rho V^2 A} \quad (14)$$

3.2. CFD Methodology and Setup

3.2.1. Domain Setup

All ground vehicle geometries were modelled by using Solidworks 2021 and were imported into Ansys Spaceclaim for domain setup and sizing. A domain sized 25 m in front, 75 m behind, 11 m above, and 11 m to the side of the vehicle was formed around the geometry, giving a blockage ratio of less than 1.5%. For the majority of the simulations, vehicle dimensions were approximately $L = 5$ m, $W = 2.2$ m, and $H = 1.6$ m. All vehicle surfaces were modelled as stationary walls, while the ground was set as a moving no-slip wall, the inlet as a velocity inlet, and the outlet as a pressure outlet. The wheels were set as moving walls with the rotating boundary condition applied to model their rotation. The model was split in half to save on size along its symmetry plane. The symmetry plane, along with the two sky surfaces, was given the symmetry boundary condition.

3.2.2. Mesh and Solver Settings

All models were meshed by using Ansys Fluent’s built-in meshing tool. The surface mesh consisted of 1–5 mm elements on bulk surfaces, with smaller elements used on finer features. The inflation layer consisted of 16 layers with a first-cell height of 0.0375 mm to ensure a y^+ of approximately 1 over the majority of the model, -as shown in Figure 1. A poly-hexcore volume mesh was grown throughout the fluid domain, with elements closest to the model being sized at 18 mm. Two coarser refinement regions of 30 mm and 42 mm existed outside this finer region. The wake regions consisted of 45 mm elements. The remainder of the domain was restricted to a max element of size 204.8 mm. Meshes generally consisted

of 35–45 million cells, enabling high-fidelity, symmetric, RANS vehicle simulations. The $k - \omega$ SST turbulence model was used to model turbulence throughout the domain. The steady-state, pressure-based, coupled, pseudo-transient solver was used with a density of 1.2215 kg/m^3 and $\mu = 1.8013 \times 10^{-5} \text{ Pas}$. The velocity inlet was set to 30.56 m/s , while the pressure outlet was set to 0 Pa gauge. For the airspeed of 30.56 m/s , the respective Re for the study was 10.63×10^6 , meaning that the flow was dominated by inertial effects and the drag coefficient would be expected to remain relatively constant for increased airspeeds [9,17,20]. The moving ground was set to 30.56 m/s in the flow direction, while the wheels rotated around their centres according to $v = \omega r$. Stationary vehicle surfaces were modelled as smooth no-slip walls. Surface roughness effects were not accounted for, as in previous work, surface roughness models with small roughness heights on exposed vehicle bodywork were found to have negligible effects on the force coefficients. Vehicle undersides and tyre surfaces were similarly modelled as smooth surfaces, which was an approximation between the real vehicles and those modelled; however, as the main area of focus was around the roof and the lightbar, the effects due to this approximation were minimised. All solver schemes were of second order. Simulations were run for 1250 iterations, with the aerodynamic coefficients being averaged over the last 500 iterations. In general, the RANS simulations converged after only 300–400 iterations. Once set up, case files were exported to 48-core HPC clusters for solving. The simulations ran for approximately 24 h each with the entire study consuming approximately 100,000 CPU hours.

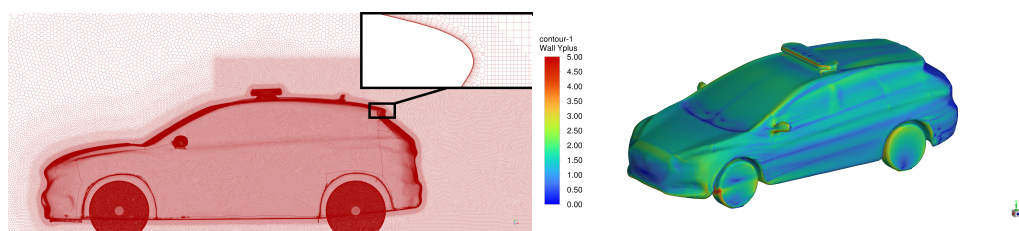


Figure 1. Image outlining the general mesh used (left) and the corresponding y^+ values on the surface of the vehicles (right).

For the hybrid LESs, the SBES model was used with the Dynamic Smagorinsky model applied as the sub-grid-scale model. The $k - \omega$ SST model was used to model turbulence for the RANS portion of the hybrid approach. A coupled pressure–velocity scheme was used with the recommended bounded central differencing applied to momentum discretisation. A first-order implicit scheme was used for the transient formulation. A refined mesh was created for the hybrid LESs, where additional refinement regions were applied around the vehicle and in its wake. In general, the cell count for these simulations was 60–70 million. Due to limitations on computational resources, half models using the symmetry boundary condition were still used even though the resolving of turbulent structures using LESs provides an inherently nonsymmetric solution. The error associated with this is limited when calculating noise at receivers away from the symmetry plane [21]. The simulations were first initialised with a RANS simulation and then allowed to run for 2640 timesteps with a timestep of $3.75 \times 10^{-4} \text{ s}$. Five inner loop iterations were used per timestep. The averaging of the flow quantities was performed for the last 3 flow passes, with the full simulation taking around 6.5 vehicle flow passes. In general, the force coefficients converged after 2 flow passes. The timestep was chosen to ensure a CFL of 1 or less around the vehicle and in its wake. There were sections very near to the vehicle where the flow was accelerated or the cell size was reduced where the CFL number rose above 1. A verification simulation with a timestep of $1.875 \times 10^{-4} \text{ s}$ was performed to confirm if the larger timestep was appropriate. The results showed a ΔC_D and a ΔC_L of only 2 counts and 4 counts, respectively, which verified that the larger timestep was sufficiently small and practical for efficient use of the computational resources [22]. Ideally, the mesh resolution for these types of transient simulations should be higher, and the number of flow passes used before and during averaging should be much higher, but due to limitations on computational

resources, this could not be achieved. Nevertheless, the results for these simulations agreed well with the results of the high-fidelity RANS simulations.

3.3. Mesh Verification Study

Table 1 outlines the results of a mesh sensitivity study performed on a Hyundai i40 (Hyundai, Seoul, Republic of Korea) estateback fitted with a lightbar. Note that vehicles outfitted with lightbars are referred to as Marked throughout this article. The baseline mesh settings which were applied to all vehicles for the RANS simulations equated to 36.2 million cells on the i40 Marked. Refined meshes R1 through to R4 outlined in Table 1 include a variety of refinements, including halving the cell size of the near vehicle volume mesh, doubling the number of inflation layers used to 32, and refining the surface mesh on the vehicle to have a maximum element size of 2.5 mm. It is clear from the results that the drag coefficient varies by approximately 1% across the various refinement methods, which verifies that the baseline mesh settings were adequately refined.

Table 1. Table showing the variation in C_D against cell count for the Hyundai i40 Marked.

Mesh Name	Original	R1	R2	R3	R4
Cell count (million)	36.2	45.9	60.4	72.9	93.0
Drag coefficient	0.2907	0.2884	0.2870	0.2878	0.2888
% difference C_D	-	-0.79%	-1.27%	-1.00%	-0.65%

3.4. Validation Study

3.4.1. Force Coefficient Validation

The average drag increase when fitting a lightbar predicted by using the CFD methodology of this article across five different police vehicles was 8.82% (see Section 4.1). Based on the estimate that fuel consumption increases are 40–50% of the drag increases [23–25], this would equate to a 3.53% to 4.41% increase in fuel consumption. Based on fuel economy data provided by the Irish police force for April 2023 (recorded for ISO50001 documentation), it was found that for 1650 police vehicles, the median fuel consumption increase for lightbar (621) vs. no-lightbar (1029) vehicles was 3.82%. The data were based on fuel economy data in l/100 km, with the median distances travelled being 1463.5 km and 2000 km for the no-lightbar and lightbar vehicles, respectively. As the dataset is prone to outliers, the median is the most appropriate measure of average. The CFD-predicted fuel increase aligns well with the values recorded in the fuel economy data for a wide range of police vehicles. Therefore, the force measurements reported in the Results section have a good degree of validation against on-road measurements.

3.4.2. Aerodynamic Noise Validation

To validate that the predicted far-field noise increases due to the lightbars were correct, a validation study based on the 2024 work by [26] was performed. The exact SAET4 square-back body provided in the research data of the article was used. A simulation domain was created around the body to match that used throughout this article, and a hybrid LES was performed with settings matching those discussed in the Methodology section above. Figure 2 outlines the geometry used and the respective locations of the receivers, while Table 2 shows the comparison between the values predicted by using this study’s CFD methodology and that of [26]. There is good agreement between the noise levels predicted in the near field of the body, as seen by the values at the first two receivers deviating by only 1.27 dB and 2.53 dB, respectively. The third receiver, which was a considerable distance away from the body, shows the highest deviation, which is acceptable, as the level of mesh refinement at this point is different between the two simulations. Additionally, the CFD work carried out by [26] draws its validation from wind tunnel tests to predict noise on this body outlined in [27,28]. Both studies identified an aeolian tone of 40 Hz at a surface probe positioned nearest the mirror, which was predicted by this study as outlined in Figure 2. Based on these results, it can be concluded that the noise predictions throughout this study

have a good degree of validation against acoustic wind tunnel data [27,28] and similarly derived published CFD work [26].

Table 2. Comparison of the overall sound pressure level at the receivers based on noise emanating from the SAET4 body, ref. [26] vs. CFD.

Receiver Locations	Validation Article (dB) [26]	CFD (dB)	% Difference
M1 (1.6, 0.92, 0.9 m)	107.67	106.40	−1.18%
M2 (1.6, 0.92, 1.8 m)	76.18	78.71	3.32%
M3 (1.6, 0.92, 3.6 m)	63.99	69.80	9.08%

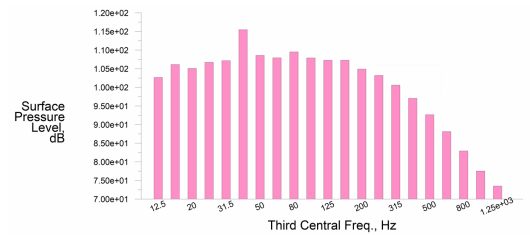


Figure 2. Image of the SAET4 square-back body with the respective receivers coloured in red (left) and the predicted surface pressure levels at a probe nearest the mirror on the SAET4 body (right).

4. Results and Discussion

4.1. Vehicle Type Dependency

To begin to understand the aerodynamic effects of fitting a lightbar to an emergency vehicle, a study to quantify the drag force increase across a variety of different vehicle types was proposed. Four police vehicles and one ambulance van were chosen based on their relevance to emergency vehicles in Ireland. The Hyundai i40 and Tucson make up a large proportion of the Irish police vehicle fleet, while the Mercedes Benz Sprinter van, due to its large size and typical van shape, makes it a highly suitable ambulance van representative. The lightbar fitted onto the vehicles was drawn to be an exact replica of those fitted onto the vehicles in Ireland. The main installer of the lightbars provided the respective CAD models for the lightbar and the technical drawings for the mounting brackets. Initially, several police vehicles were measured to ensure that the lightbars fitted in the CAD models were installed at the same height and position as those fitted onto the real-life police vehicles. The models for the cars were prepared in ANSYS SpaceClaim by using online scanned models for the cars and wrapped to have all the relevant external features, except for a detailed underside, internal flow, and detailed wheels. Figure 3 outlines the five emergency vehicles fitted with their respective lightbars. Table 3 describes the drag force increases for each vehicle when fitted with a lightbar.

There was a common trend among the four police vehicles, whereby the drag force increment was approximately 8–11%. The vehicle with the highest drag increase was the i40, which was expected, as it represents the saloon vehicle type, whereas the Tucson had the lowest increase due to its larger shape being less perturbed by the addition of the lightbar. It is crucial to note that the drag force increases reported are generally not that large, meaning the additional fuel expense for adding a lightbar to these vehicles is not inhibitive. If, however, the police vehicle were a notchback- or fastback-styled saloon, then the drag increase would be higher, as the disturbed flow behind the lightbar would interact poorly with the sloping roof to give a large pulling force on the rear-facing surfaces of the vehicle. The five vehicles studied here all had straight backs; hence, the drag force increments were not severe. This is an important consideration for fleet managers, as, if planning to buy a specific vehicle to be fitted with a lightbar, the priority would be to have a straight-back vehicle rather than a sloped-back vehicle.

Table 3. Drag increases for the five baseline vehicles when fitted with a lightbar (M = Marked).

Vehicle Type	C_D	C_D % Change	Area (m ²)	Area % Change	Drag Change
Hyundai i40 Estate	0.272	-	2.23863	-	-
Hyundai i40 Estate M	0.291	7.0 %	2.30710	3.1 %	10.3 %
Hyundai Tucson	0.301	-	2.50334	-	-
Hyundai Tucson M	0.316	5.0 %	2.57175	2.7 %	7.9 %
Kia EV6	0.262	-	2.38501	-	-
Kia EV6 M	0.276	5.3 %	2.45360	2.9 %	8.4 %
Mercedes Benz Sprinter	0.294	-	4.49784	-	-
Mercedes Benz Sprinter M	0.314	6.8 %	4.56636	1.5 %	8.4 %
Hyundai Kona	0.315	-	2.26110	-	-
Hyundai Kona M	0.332	5.4 %	2.33961	3.5 %	9.1 %



Figure 3. Rendered image of the five baseline Marked vehicles fitted with lightbars.

Another reason why the drag increments shown are generally quite low is due to the low-profile shape of the current generation of lightbars used today on police vehicles. Figure 4 shows how the flow has a relatively easy path around the lightbar, as it is accelerated above and below the lightbar, with the highest speeds being reached underneath. The wake behind the lightbar is not extensive; hence, the flow can partially reattach downstream on the roof. Figure 5 shows the small extent of the lightbar’s wake in the total pressure isosurface, while the q criterion isosurface shows the many vortex structures that form after the lightbar. The most significant are those at the sides of the lightbar, which then angle inward and enable some flow reattachment on the roof. The right image in Figure 6 shows how attachment at the sides of the roof is enhanced vs. that at the centre of the roof due to the vortices behind the lightbar. The pressure field around the lightbar is of great importance in the context of drag. The left image in Figure 6 outlines how the front of the lightbar has significant flow stagnation, but as the frontal area is quite small, the resulting drag force is reduced. Due to the flow acceleration above and below the lightbar, very-low-pressure zones are seen in these regions. The effect of the lightbar is felt upstream, as a high-pressure zone is created in front and travels an appreciable distance until it reaches the very-low-pressure zone observed at the point where the windscreen meets the roof.

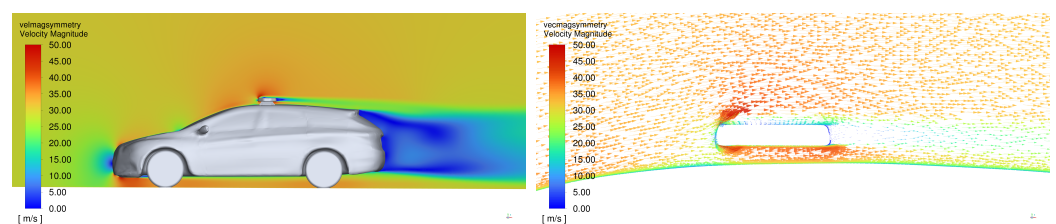


Figure 4. Velocity magnitude plots along the symmetry plane of the i40 Marked.

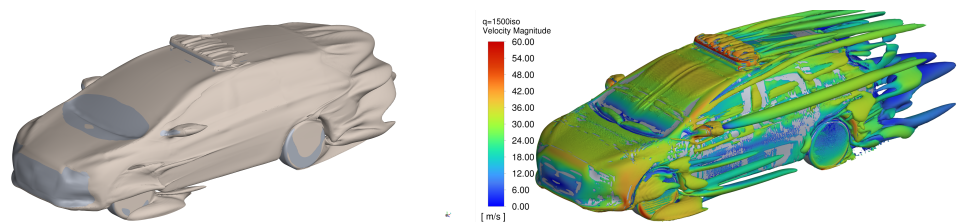


Figure 5. Flow field visualisation around the i40 Marked with total pressure = 0 Pa (left) and q criterion = 1500 s^{-2} isosurfaces (right).

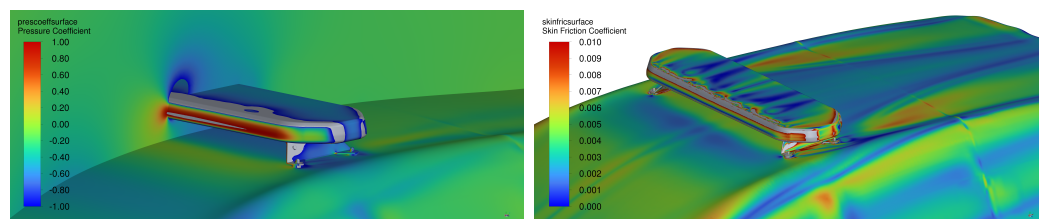


Figure 6. Surface flow visualisation on the i40 Marked with pressure coefficient (left) and skin friction coefficient contour plots (right).

To further highlight how the drag force increments for the lightbar across the different police vehicles were similar, drag force reports on specific vehicle surfaces were created to observe where the drag count changes occurred due to the lightbar's presence. The trend was that the total drag count increment for all four vehicles was approximately 14–16 counts. Looking at the surface-specific reports, it showed that the lightbar's surfaces were responsible for 12–14 counts of additional drag while the roof's surfaces had an 8–9-drag count increase. The increase in roof drag is an interesting effect of adding a lightbar to a vehicle. It is primarily due to the high-pressure zone ahead of the lightbar slowing the flow and reducing the thrust force present on the forward-facing surfaces of the roof ahead of the lightbar. Additionally, it is due to the rearward surfaces of the roof which are exposed to a lower-pressure flow in the wake of the lightbar, resulting in additional drag. This drag increase totalled 20–21 counts but was then offset by slight drag reductions on other vehicle surfaces. One surface which had an approximate 2-count reduction across all vehicle types was the rear, which benefited from the slowed flow after the lightbar-induced separation with lower energy and producing slightly higher pressured wake. Interestingly, the vehicle's frontmost surface also experienced a consistent drag reduction of 2–2.5 counts across all vehicle types. The proposed reason for this is down to the high-pressure zone in front of the lightbar being felt far upstream and providing a forward pushing force to the flow as it stagnates on the vehicle front. Note that this effect was very small, and for context, this 2–2.5 reduction occurred on a surface responsible for 70–130 counts of drag. Lastly, other surfaces had slight drag reductions due to the lightbar's presence; for example, the back wheels consistently showed a slight 1-drag count reduction. All this leads to the conclusion that the drag force increment due to the same lightbar is consistently similar on all straight-back vehicles.

4.2. Lightbar Positional Study

To further understand the aerodynamics of the external lightbar, it was crucial to look at how its mounting position affects the drag increases on the vehicle. The main considerations are those around the height of the lightbar above the roof, the orientation of the lightbar, and the chosen mounting pillar to fit the lightbar. Figure 7 outlines the geometries simulated in the positional study. The standard lightbar's height above the vehicle was chosen based on measurements taken from real-life police vehicles fitted with lightbars. Three alternative height configurations were proposed to observe the resulting drag force changes. i40 M-Lowest had a height 42 mm lower than the standard, which resulted in minimal roof clearance at the centre of the lightbar. As the roof of the i40 is curved, the clearance increased towards the left and right ends of the lightbar. i40 M-Lowered had a height reduction half

of that of i40 M–Lowest. Finally, i40 M–Higher had an additional 45 mm of roof clearance and was sized according to what visually looked like the maximum height at which a lightbar would be fitted for practical reasons.



Figure 7. A rendered image of the positional changes to the standard lightbar on the Hyundai i40.

The lightbar’s orientation was adjusted by 90 degrees in i40 M–Longitudinal to see what the drag benefits would be for such a configuration. To facilitate this, the same mounting brackets fitted to the standard lightbar were moved inwards, so that it could be mounted similarly to the standard configuration. Lastly, the location at which the lightbar was fitted was studied, as the current practice is to always fit it at the B pillar, even though the Hyundai i40 has two other pillars (C and D) available for mounting. No mounting configuration for the A pillar was set, as the drag is expected to increase considerably based on the information gathered in the literature review and because of practical reasons due to a lack of structural support for the mounting bracket and enhanced roof curvature at this location. Table 4 outlines the results of the positional study.

Table 4. Drag changes for the positional changes to the standard lightbar on the Hyundai i40.

	C_D	C_D % Change	Area (m ²)	Area % Change	Drag Change
i40 M–Lowest	0.292	0.3%	2.30589	−0.1%	0.3%
i40 M–Lowered	0.293	0.7%	2.30620	0.0%	0.6%
i40 M–Standard	0.291	-	2.30710	-	-
i40 M–Higher	0.321	10.3%	2.30754	0.0%	10.3%
i40 M–Longitudinal	0.282	−3.1%	2.26112	−2.0%	−5.0%
i40 M–C Pillar	0.291	0.0%	2.30674	0.0%	0.0%
i40 M–D Pillar	0.290	−0.3%	2.30586	−0.1%	−0.4%

The most surprising result from Table 4 is that lowering the lightbar from the standard position does not reduce drag. Instead, very slight drag increases were reported of the order of less than 1%. The reason for this can be explained by looking at the individual drag reports for the specific vehicle surfaces. Lowering the lightbar to its lowest point led to a reduction of just under 1.5 drag counts on the lightbar’s surface. This was primarily due to the mounting mechanism in its condensed form still generating a notable amount of drag as the flow accelerates under the lightbar and meets the mounts. This is then combined with an approximately 1-drag count reduction at the rear of the vehicle due to the slower flow in the wake of the lightbar. Again, this 1-count reduction at the rear is very small in the context that the rear of the i40 totals 75 counts of drag over its rear and rear glass. These reductions are then offset by drag increases on the roof, where an enhanced high-pressure zone ahead of the lightbar further reduces the amount of thrust developed on the forward-facing parts of the roof. Figure 8 demonstrates the extent of this enhanced high-pressure zone in comparison to that seen in Figure 6 for the standard lightbar. The resulting roof drag increases equate to 3 counts, which is why lowering the lightbar did not reduce drag as expected but instead very slightly increased it.

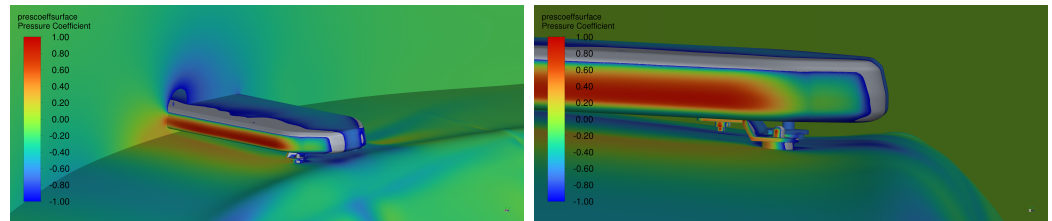


Figure 8. Pressure coefficient contour plots on i40 Marked-Lowest.

In contrast, raising the lightbar to the higher position gave an expected 10.3% drag increase over the standard lightbar configuration. It is interesting to note that the location at which the drag increased substantially was not around the lightbar but instead downstream at the rear of the vehicle. The lightbar's surfaces had only a 0.5 count increase due to their placement in the raised position; however, the extent to which the flow was disturbed because of the new position was seen to increase the drag on the rear glass of the vehicle by 23.5 counts and by 4.5 counts on the general rear of the vehicle. When combined with a slight drag increase on the roof of 1.5 counts, which resulted from increases downstream of the lightbar and not upstream, the net drag increase for this higher position was 30 counts. The left image in Figure 9 shows how the wake of the i40 was substantially altered due to the new lightbar position and is noticeably different from that in Figure 4 near the vehicle's rear glass. Not shown in the figures is the isosurface of the Q criterion, which showed how the flow separating at the end of the roof had additional strong turbulent vortices that helped produce the substantially lower base pressure on the vehicle's rear glass.

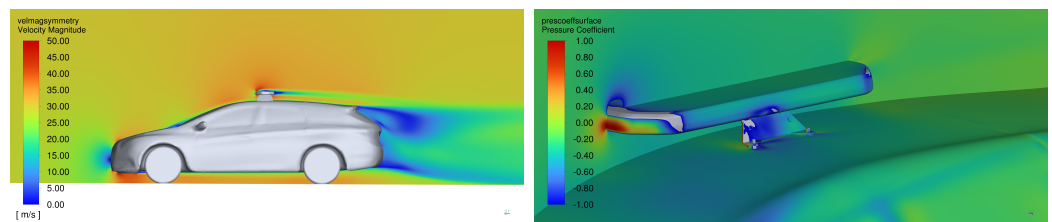


Figure 9. Velocity magnitude plot along the symmetry plane of i40 Marked-Higher (left) and pressure coefficient contour plot for i40 Marked-Longitudinal (right).

The best-performing positional change, as expected, was to reorientate the standard lightbar longitudinally while maintaining the same mounting mechanism for fairness in the comparison. A total drag reduction of 5% was reported; it primarily came from the 10-drag count reduction reported for the lightbar's surfaces. Additionally, the roof drag component was reduced by 4 counts, as the high-pressure zone ahead of the lightbar became significantly diminished and enabled enhanced thrust on the forward-facing parts of the roof, as seen in the right image in Figure 9. These savings are then slightly offset by a 3-drag count increase at the rear of the vehicle due to faster-moving flow on separation and a 1.5-drag count increase at the i40's front, which comes from the removed benefit outlined in Section 4.1 of having a high-pressure zone ahead of the lightbar that affects the stagnation flow upstream. Combined with small miscellaneous changes on other surfaces totalling a 0.5-drag count increase, the configuration had a net 9-drag count decrease. Lastly, based on the results in Table 4, it is clear that for a straight-back vehicle like the Hyundai i40 estate, mounting the lightbar on the C and D pillars had approximately the same drag effect as when mounting on the B pillar. This was again down to the low-drag nature of the standard lightbar and because of the straight-back roof on the vehicle. If, however, this configuration were applied to a vehicle with a rearward-sloping roof, mounting the lightbar further back would give rise to substantial drag increases, as the disturbed flow field after the lightbar would negatively affect the drag forces on these sloped surfaces, similar to what was outlined in [9].

4.3. Simplified-Lightbar Study

As the lightbar discussed in the previous was based on a fully detailed lightbar with realistic mounting brackets and a rectangular profile produced by a manufacturer, it was of interest to see how a simplified version of this lightbar would perform aerodynamically. The top left image in Figure 10 shows the baseline simplified lightbar mounted on the Hyundai i40. The simplified lightbar had identical dimensions to its detailed equivalent with the only exception being its simplified mounting bracket and slightly more rectangular profile. The simplified mounting bracket was modelled as an oblique rectangular prism with overall width and length based on the outer limits of the detailed bracket. The baseline simplified lightbar was then modified as per Figure 10 to investigate the aerodynamic effects of angling it into the flow, lowering it, and removing its mid-section. Table 5 outlines the drag changes for each configuration.

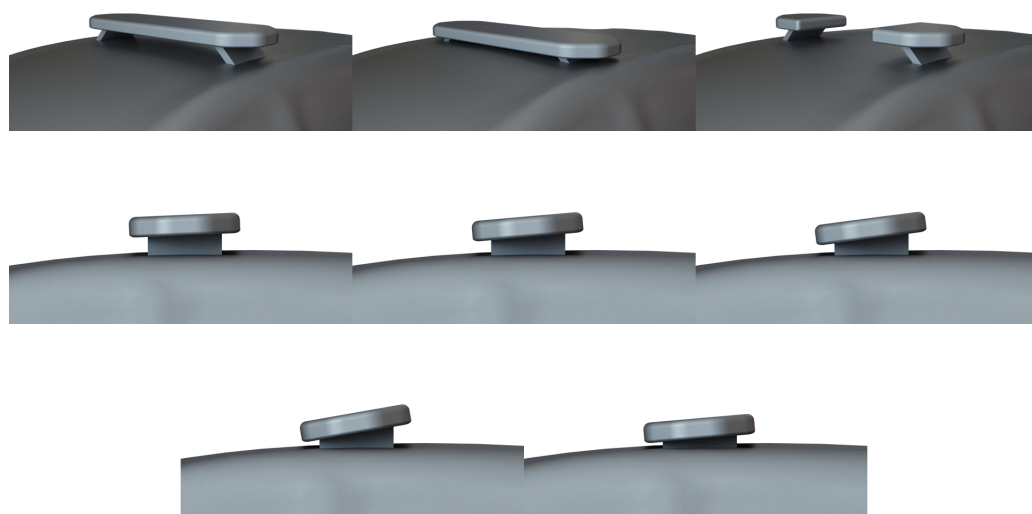


Figure 10. Rendered images of the simplified lightbar configurations on the Hyundai i40. The image order matches the order of Table 5.

Table 5. Drag changes for the simplified-lightbar configurations on the Hyundai i40 (SL = simplified lightbar).

	C_D	C_D % Change	Area (m ²)	Area % Change	Drag Change
i40 M SL	0.290	-	2.31011	-	-
i40 M SL–Lowest	0.284	−2.1%	2.30640	−0.2%	−2.2%
i40 M SL–Split	0.289	−0.3%	2.28049	−1.3%	−1.6%
i40 M SL–2.5°	0.289	−0.3%	2.32185	0.5%	0.2%
i40 M SL–5°	0.297	2.4%	2.33353	1.0%	3.5%
i40 M SL–7.5°	0.311	7.2%	2.34524	1.5%	8.9%
i40 M SL–10°	0.320	10.3%	2.35682	2.0%	12.6%
i40 M SL–5°–Lowered	0.293	1.0%	2.33126	0.9%	2.0%

As the results in Table 5 highlight, the simplified lightbar (0.290) had effectively the same drag properties as the detailed lightbar (0.291), with a C_D variation of only 1 count. Both lightbars reported a drag force of 14 counts, with the net 1-count difference coming from a slight drag reduction at the rear of the vehicle, most probably due to the smoother flow behind the simplified lightbar. The most notable result from the study was that lowering the simplified lightbar reduced drag by 6 counts, in contrast to what was outlined in the previous section for a detailed lightbar. This reduction was effectively all generated on the surfaces of the lightbar, which reported a 5.5-count reduction due to lower forces generated from the mounting mechanism in its condensed form. The crucial conclusion from this is that lowering a lightbar can reduce drag if the mounting mechanism used is

sufficiently clean to not cause excessive flow disturbances underneath the lightbar as the flow is accelerated in the reduced gap.

The split lightbar design offered a marginal 1.6% drag reduction, with the reduced frontal area of the lightbar being the primary cause for the reduction. The reduction was not due to the Marked vehicle becoming more aerodynamic, as only a 1-drag count reduction was reported compared with the baseline simplified lightbar. Looking at the specific surfaces, the lightbar’s drag was reduced by 4 counts, while the roof also reported a 4.5-count reduction. These were then offset by drag increases at the rear (5 counts), due to faster flow separation at the rear, and at the front of the vehicle (1.5 counts), due to the reduced stagnation ahead of the lightbar not having a pushing effect that filtered upstream as much. Combined with misc increases elsewhere totalling 1 count, the net 1-drag count reduction was achieved. This leads to the conclusion that the savings for a split lightbar design are not substantial enough to justify its usage over the standard full-length rectangular lightbar.

Angling the lightbar was shown to increase drag for angles above 2.5°, whereas a lightbar angled at 2.5° was shown to have a negligible drag increase. This is of great practical significance, as when installing a lightbar, it may be necessary to angle it slightly to suit the curvature of the roof or for noise reduction based on empirical testing. Therefore, angling the lightbar slightly for these purposes should not have a noticeable impact on fuel economy. For more aggressive angles, it was shown to increase drag by approximately 4% for every additional 2.5°. The cause of the drag increase was primarily drag originating from the rear of the vehicle and on the lightbar itself. For example, the 7.5° configuration had a 21-drag count increase, of which two-thirds originated from the rear of the vehicle and one-third from the lightbar’s surfaces. This substantial increase in rear drag results from the more turbulent non-smooth flow in the wake of this aggressively angled lightbar, which then connects with the vehicle’s main wake to produce lower base pressures. Lastly, lowering an aggressively angled lightbar reduces the resulting drag penalty, as was shown for the 5° configuration, where a 4-count reduction was realised for lowering it from its baseline height.

4.4. Previous-Generation Lightbar

As shown in the preceding sections, the modern low-profile lightbar does not add inhibitive amounts of drag to straight-back emergency vehicles, owing to its well-designed aerodynamic shape. For context, an older-generation lightbar as shown in the left image in Figure 11 was simulated to quantify the drag savings between the new- and previous-generation lightbars. Its design was based on images of lightbars used on various police vehicles in years past. This type of lightbar is still used today by some emergency service vehicles around the world, especially on vehicles where visibility is a priority. Table 6 outlines how this style of lightbar increases baseline drag by nearly 22%, double that of the current-generation lightbar. The result aligns well with a 2008 news article [29] that described a wind tunnel study where 8–10% drag savings were found for New Zealand’s police vehicles when fitted with the new slimline lightbars over the older bulkier ones. The geometries discussed are a good match to those simulated, offering an added level of validation to the results. There was no accompanying peer-reviewed article for the news story, as is common practice when police carry out wind tunnel work for their vehicle aerodynamics, reinforcing the need and the literature gap for this article.

Table 6. Drag force increase for previous-generation lightbar on Hyundai i40.

	C_D	C_D % Change	Area (m ²)	Area % Change	Drag Change
Hyundai i40 Estate	0.272	-	2.23863	-	-
Previous-Gen Lightbar	0.313	15.1%	2.36729	5.7%	21.7%

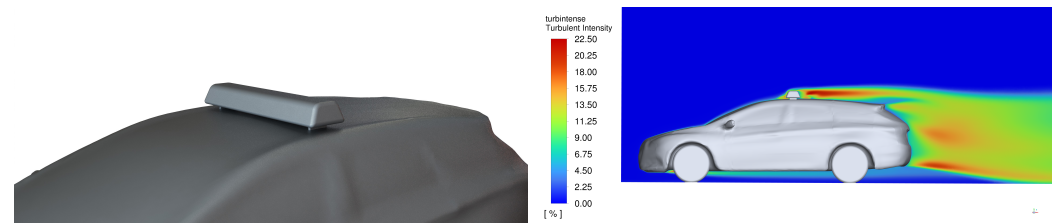


Figure 11. Rendered image (left) and turbulent intensity contour plot (right) for previous-generation lightbar on Hyundai i40.

The cause of the added drag on the previous-generation lightbar over the newer one primarily originates from drag increases over the rear glass of the i40. The 22 counts of added drag between the old (0.313) and new (0.291) lightbars were reached based on increases at the rear glass, roof, and lightbar surfaces to the values of 13, 8, and 4.5 counts, respectively. The right image in Figure 11 shows the substantial amount of turbulence in the wake of the lightbar, which was why the base pressure behind the lightbar and on the rear glass was noticeably reduced. The 8-drag count increase at the roof was primarily due to some reduced thrust on the roof in front of the lightbar and to the under-pressured wake of the lightbar exerting a pulling force on the slightly sloped rear roof of the estateback. It is crucial to highlight that if this lightbar were fitted onto a notchback or fastback police vehicle, then the roof drag increase would be much greater, as the low-pressure lightbar wake would have considerably more rear projected area to exert a pulling force on. Interestingly, the older lightbar surfaces had only a 4.5-count increase compared with their newer version, which was due to the front shape of the older lightbar being conducive to increases in thrust, which was then offset by increases in rear-lightbar drag, netting 4.5 counts. Lightbars such as this would be much less suited for electric vehicles, as the range detriment is expected to be double that of the newer slimline versions.

4.5. Drag-Reducing-Ramp Study

A drag-reducing-ramp study was proposed based on the results of [9], where substantial drag reductions were realised through the utilisation of an aero ramp ahead of a protrusive taxi sign. The goal was to see if a ramp could be used to alter and improve the flow's paths as it transverses the lightbar to reduce stagnation, slow the flow, and reduce the turbulence that occurs downstream of the lightbar. This was all to be achieved while minimising the self-drag component on the ramp so as not to offset any drag savings on the lightbar. Figure 12 shows the eight different ramp designs that were tested, while Table 7 outlines their respective drag changes. As it is clear from the table, all eight designs failed to reduce the base drag on the Hyundai i40 Marked. The key issues were that the ramps in most cases increased the roof drag component and in some cases caused noticeable drag increases at the rear of the vehicle due to the increase in the size of the wake behind the lightbar and the increase in the level of turbulence downstream of it. This was especially true for the worst-performing ramps. For example, DRR 7 did succeed in reducing the drag on the lightbar by 12 counts but then offset this by 9 counts due to ramp self-drag, followed by a large 11-drag count increase at the roof and a 16-count increase at the rear of the vehicle. Both the rear and roof drag increases were resulted from detached turbulent airflow after the ramp, which is clearly shown in the left image in Figure 13.

DRR 3 performed notably better, having a near-zero self-drag component due to the front curvature of the ramp facilitating considerable levels of thrust, combined with reduced rear ramp drag from a positive interaction with the high-pressure zone ahead of the lightbar. The key advantage of DRR 3's design was that it reduced lightbar drag by 9 counts without detrimental drag increases at the rear of the vehicle. The downside was that it increased roof drag by 12 counts for the usual reasons of reducing the roof's forward-facing surface thrust and lowering the pressures on the rear roof, enhancing the rearward pulling force. Generally, the best design was DRR 2, where having a depression/notch at its centre solved the added roof drag problem, enabling it to increase roof drag by only

1 count. The downside of the design was that it had substantial self-drag (11 counts) due to its abrupt trailing edge facilitating low-pressure wake at its edges. DRR 2 offered a 9-drag count reduction at the lightbar and notably offered a 1-drag count reduction at the rear of the vehicle. This was brought about by slightly less turbulent flow on the rear roof due to the lightbar–ramp combination. The right image in Figure 13 outlines the improved flow after DRR 2 along the symmetry plane.

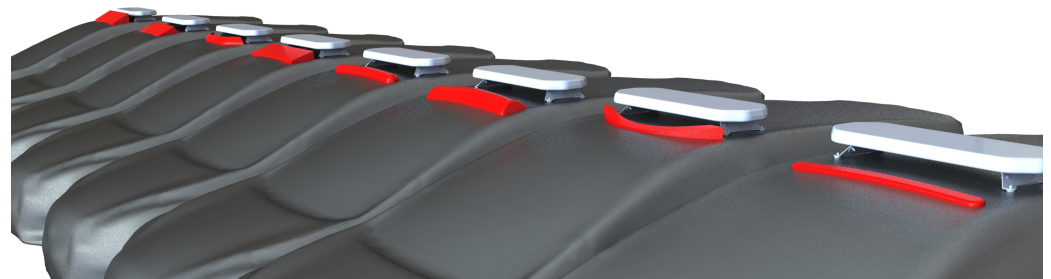


Figure 12. A rendered image of the drag-reducing ramps (DRRs) fitted onto the Hyundai i40 Marked. Ramps are ordered based on their drag increases from right to left and labelled 1 to 8 as per Table 7.

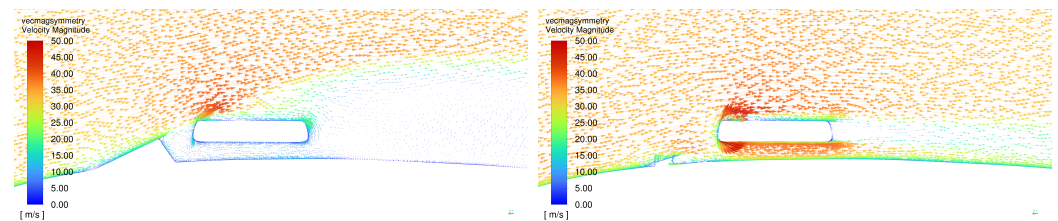


Figure 13. Vector plots of velocity magnitude along the symmetry planes of DRR 7 (left) and DRR 2 (right).

Table 7. Drag changes for the various drag-reducing ramps fitted onto the Hyundai i40 Marked. The order from top to bottom in the table matches the geometry from right to left in Figure 12.

	C_D	C_D % Change	Area (m ²)	Area % Change	Drag Change
i40 M–DRR 1	0.294	1.0%	2.30801	0.0%	1.1%
i40 M–DRR 2	0.292	0.3%	2.33187	1.1%	1.4%
i40 M–DRR 3	0.293	0.7%	2.34248	1.5%	2.2%
i40 M–DRR 4	0.299	2.7%	2.33476	1.2%	4.0%
i40 M–DRR 5	0.303	4.1%	2.35892	2.2%	6.5%
i40 M–DRR 6	0.309	6.2%	2.35229	2.0%	8.3%
i40 M–DRR 7	0.313	7.6%	2.35365	2.0%	9.7%
i40 M–DRR 8	0.338	16.2%	2.36072	2.3%	18.9%

The main conclusion to draw from this is that fitting a ramp ahead of a low-drag lightbar is generally not a good approach and is very likely to increase vehicle drag. This is a notable consideration for emergency vehicles that are fitted with ramps or angled units ahead of their lightbars for noise reduction or lighting. For future work, it would be of interest to produce a hybrid ramp design based on DRR 2 and DRR 3, which incorporates the low self-drag of DRR 3 and the reduced roof drag of DRR 2.

4.6. Hybrid-LES Results

As a high number of configurations were simulated in this article, an entirely hybrid-LES approach was not feasible due to the significantly increased computational expense of transient simulations. For comparison, only the i40 Marked and Kona Marked were simulated by using the hybrid-LES approach discussed in the Methodology section. As Table 8 outlines, the overall C_D predictions for both methods were reasonably similar; however, some discrepancies were observed when viewing the individual contributions

from some vehicle surfaces. The largest deviations were reported at the front wheels and surrounding areas along with the rear of the vehicles. For example, for the i40, a 17-force count decrease was seen at the front wheels and surrounding wheel wells, which was then offset by a 10-force count increase at the rear of the vehicle. This result is in line with previous works that found similar deviations on these surfaces [14,15]. Most importantly, there was excellent agreement between the force predictions for the roof and lightbar for both approaches, with a maximum deviation of only 2 counts for the self-drag component of the lightbar. This provides a high level of confidence in the predicted drag changes outlined for the different lightbar configurations throughout this article using the RANS methodology.

Table 8. Differences in C_D for the RANS and hybrid-LES approaches for the i40 and Kona Marked.

	RANS	Hybrid LES	C_D % Change
Hyundai i40 Marked	0.291	0.286	−1.7%
Hyundai Kona Marked	0.332	0.328	−1.2%

4.7. Lightbar Noise Predictions

Using the transient results discussed in the previous section, the far-field noise levels were predicted by using the Ffowcs Williams and Hawkings model at six different receivers, as outlined in Figure 14. The locations for the receivers were carefully correlated so that the positions shown for the Kona were also those shown for the i40, as the exact (x,y,z) coordinates for the receivers were different, as the lightbar and B pillar were located differently between the SUV and the sedan. Based on the results in Table 9, it is clear that for receivers 3–6, the noise levels for both the SUV and sedan police vehicles were the same; however, a greater level of noise was seen ahead of and behind the lightbar for the SUV. For example, for the Kona, a substantial 8 dB increase was seen between the front and rear of the lightbar, with the rear reporting a very noisy 103.6 dB. This highlights that most of the noise production associated with the lightbar comes from its rear surfaces, which is in good correlation with the drag force predictions, which found the rear of the lightbar to be responsible for the highest level of drag force. The main conclusion is that if noise reduction is necessary, modifying the rear of the lightbar by using an appendable device (as discussed next in Section 4.8.2) would be the most feasible approach, as fitting noise-reducing ramps ahead of the lightbar is likely to increase drag. The design of future-generation low-noise lightbars would, therefore, primarily focus on modifying the rear of the lightbar to reduce the noise intensity associated with the lightbar’s wake and rear separation regions.

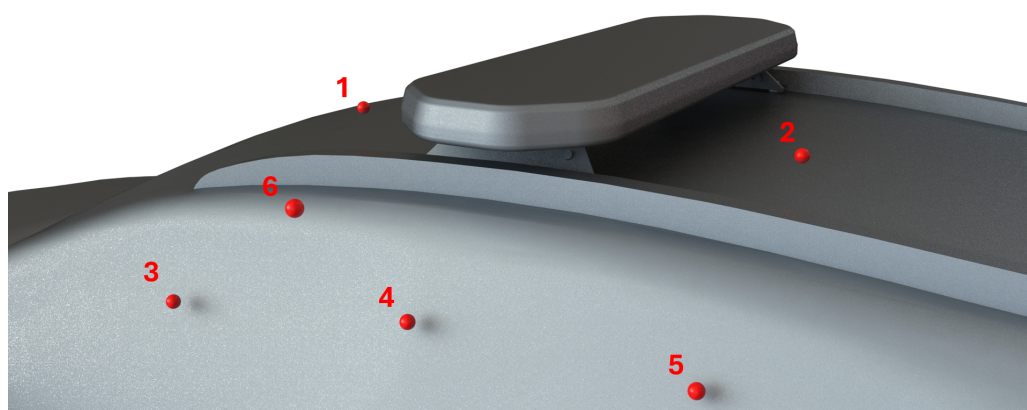


Figure 14. Noise receiver locations in the vicinity of the lightbar on the Hyundai Kona Marked.

Table 9. Overall sound pressure level (dB) at the six receivers shown in Figure 14 for the Hyundai i40 and Kona Marked.

Receiver	1	2	3	4	5	6
Hyundai i40 Marked (dB)	94.0	100.5	97.0	97.3	96.8	90.2
Hyundai Kona Marked (dB)	95.7	103.6	97.8	96.6	96.0	90.7

4.8. Low-Drag-Lightbar Study

4.8.1. Initial Designs

While the results so far have indicated that the current generation of lightbars, which uses a standard low-profile rectangular section, has adequately low drag, it is of interest to investigate how the drag could be reduced when using a modified lightbar profile. This is especially important to police departments and emergency services that have set targets for emission reductions and would consider including a specification for a more aerodynamic lightbar profile in their next tender to suppliers. To begin, four initial alternative profiles were investigated, as shown in Figure 15. V1 and V2 were designed to direct flow over the top of the lightbar, whereas V3 and V4 encouraged flow underneath the lightbar by using airfoil-like shapes. All lightbars were fitted to the Hyundai Kona, and for fairness in the comparison, the same mounting brackets and mounting positions were maintained for all configurations. The overall dimensions were similarly preserved, except for their stream-wise lengths, which increased slightly over the baseline lightbar to facilitate pointed ends at the front and rear of the lightbar.

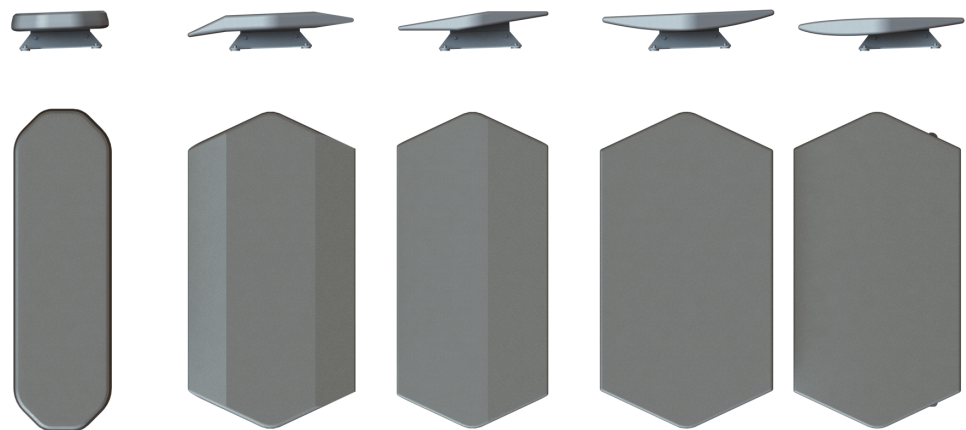


Figure 15. A rendered image of the initial low-drag-lightbar designs fitted onto the Hyundai Kona Marked. Designs are ordered from left to right according to Table 10.

The first point to observe from Table 10 is that the lightbars that encouraged the flow underneath increased drag, whereas the lightbars that encouraged the flow over the top reduced drag. V1 performed the best, offering a near 4% drag reduction over the baseline lightbar. In terms of component drag, this was made possible due to V1’s design halving the self-drag component of the lightbar. This was then combined with a roof drag reduction of 4.5 counts owing to the reduced frontal stagnation ahead of the lightbar because of its pointed front. V2, however, did not reduce lightbar self-drag, as its rearward diffusing shape still enabled a considerable pulling force on the lightbar due to large under-pressured wake. The large diffuser angle of the lightbar led to flow separation mainly near the ends of the lightbar approaching the mounting brackets. V2’s benefit did, however, lie in its ability to reduce the roof drag on the vehicle, totalling 9 counts, which was due to its optimal front-end design diverting flow over the lightbar and minimising frontal stagnation, enhancing thrust over the front-facing parts of the vehicle’s roof. V2 also reported a slight 2.5-drag count increase at the base of the vehicle, which was created by the increased levels of turbulence in the flow downstream of the lightbar. Having a rear diffuser shaped like V2 is

generally not a good design, as it overly redirects the flow upwards and away from the curvature of the rear roof, leading to increased levels of turbulence in the flow.

Table 10. Drag changes for the initial low-drag lightbars (LDL) fitted onto the Hyundai Kona Marked.

	C_D	C_D % Change	Area (m ²)	Area % Change	Drag Change
Hyundai Kona M	0.332	-	2.33961	-	-
Kona M-LDL V1	0.318	−4.2%	2.35017	0.5%	−3.8%
Kona M-LDL V2	0.325	−2.1%	2.33347	−0.3%	−2.4%
Kona M-LDL V3	0.351	5.7%	2.34067	0.0%	5.8%
Kona M-LDL V4	0.343	3.3%	2.32958	−0.4%	2.9%

This was especially true for V3 and V4, where their rear shapes effectively led to 16- and 15.5-drag count increases at the base of the vehicle, primarily due to this flow-redirecting issue enhancing turbulence. Additionally, the flow acceleration that occurred underneath these lightbars further contributed to the increase in the levels of turbulence observed downstream of these lightbars. Figure 16 highlights how downstream of V3, the turbulence intensity levels were much greater than those seen for V1’s design. Another trend for V3 and V4 was how both lightbars increased the roof drag increment by approximately 2 counts, which was caused by their wake’s flow having reduced pressure and exerting additional pulling force on the rearward-sloping roof of the Kona. The main reason why V4 had only half the drag increase of V3 was due to its inherently low-drag airfoil shape, which cut the self-drag component in half by 7 counts, similar to V1. V3, in contrast, increased self-drag over the baseline lightbar by 1.5 counts, as its upward-sloping rear had notable separation at the ends approaching the mounting brackets but was fully attached near the symmetry plane. The most important conclusion to draw from this is that even if a low-drag profile, such as that used by V4, is incorporated in the lightbar’s design, vehicle drag may not be reduced over a standard rectangular profile, as the drag reductions seen at the lightbar’s surfaces could be offset completely by increases at the roof and base of the vehicle. This would be particularly the case where the lightbar’s profile encourages underflow and diffuses upwards excessively at its rear.

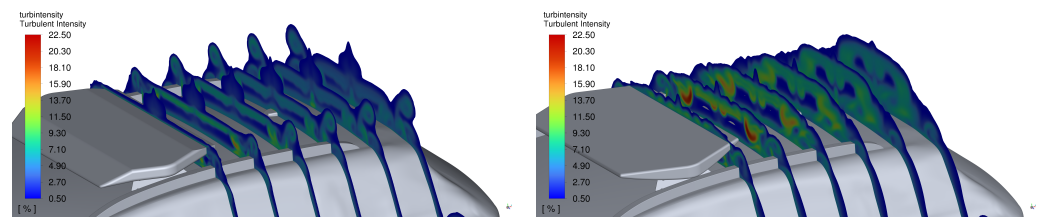


Figure 16. Plots of turbulent intensity in the lightbar wake of LDL V1 (left) and LDL V3 (right).

4.8.2. Clip-On Sections Based on LDL V1 Design

The low-drag lightbars (LDLs) of the previous section have the disadvantage of necessitating the purchase of a completely new lightbar to replace the baseline model. As LDL V1 was the best-performing design, a new clip-on study was performed to see if the reductions shown for LDL V1 could be realised with front and rear clip-ons attached to the baseline lightbar. The clip-ons would be clear adhesively mounted sections made from a similar material to the lightbar, with the advantage of not obstructing the light emitted. Their side profile matches that used by LDL V1. Figure 17 shows both clip-ons mounted to the baseline lightbar, while Table 11 highlights their respective drag changes. The results show that using only the front clip-on increases vehicle drag by 3.7%, with 0.6–0.7% of this being attributable to an area increase brought on by the front clip-on angling downwards. Post-processing showed that the self-drag component for the combination was identical to that of the baseline lightbar, offering no drag benefit. The 10-drag count increase was created by the enhanced levels of turbulence behind the lightbar, as the front clip-on’s edge

disturbed the flow and the absence of the rear clip-on produced a more turbulent wake flow that reduced the vehicle’s base pressure, causing an increase of 10 counts of rear drag.

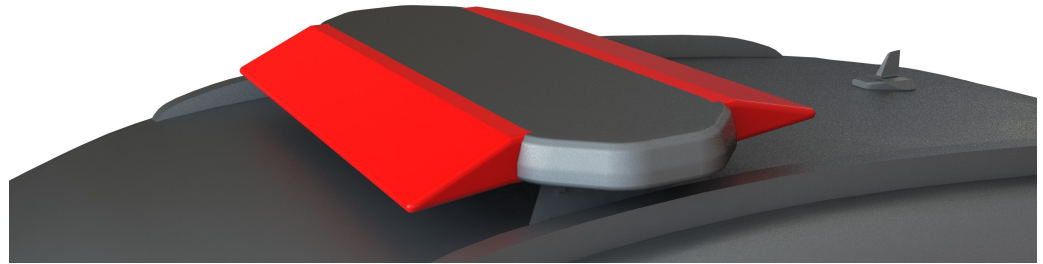


Figure 17. A rendered image of the front and rear clip-on sections fitted to the baseline lightbar on the Hyundai Kona Marked.

Table 11. Drag changes for the clip-on sections to the baseline lightbar on the Hyundai Kona Marked.

	C_D	C_D % Change	Area (m ²)	Area % Change	Drag Change
Hyundai Kona M	0.332	-	2.33961	-	-
Kona M–Front Clip-On	0.342	3.0%	2.35463	0.6%	3.7%
Kona M–Rear Clip-On	0.324	−2.4%	2.34044	0.0%	−2.4%
Kona M–Both Clip-Ons	0.322	−3.0%	2.35547	0.7%	−2.4%

Using only the rear clip-on, in contrast, reduced drag by nearly 2.5%, as it greatly reduced the wake intensity behind the lightbar. The lightbar and rear clip-on together reported a 4-self-drag count reduction, as the rear drag component of the lightbar was significantly reduced. Additionally, the rear roof and rear surfaces of the vehicle reported drag reductions of 1 and 3 counts, respectively, benefiting from reduced turbulence levels in the wake flow of the lightbar. It is interesting to highlight that the remaining 10 counts of drag still on the lightbar combination was entirely borne by the rear clip-on, as all other lightbar surfaces together reported net zero drag due to stagnation and thrusting effect offsetting. The aerodynamic noise production of the lightbar would also be significantly reduced, as the presence of the rear clip-on reduces the separation intensities and pressure fluctuations on the aft surfaces of the lightbar. Based on these results, it is reasonable to stipulate that the next generation of low-drag lightbars should have a rear section matching that of the rear clip-on discussed here. In terms of retrofitting, it provides an approximate 2.5% drag reduction for the entire vehicle through a simply constructed, easily mounted add-on. Crucially, the rear-mounted part will not interfere with the light emitted from the front of the lightbar, as front lighting is the most essential visibility requirement for emergency service vehicles. Finally, both clip-ons used together did offer an additional reduction in C_D but did not reduce drag beyond that of the rear clip-on alone due to the area increment of the front clip-on. Therefore, priority should be given to fitting only the rear clip-on.

4.8.3. Low-Drag-Lightbar Final Design

Based on the results of the previous sections, a final low-drag-lightbar design was established as shown in Figure 18; it maintains the optimal rear design of LDL V1 with an alternative front, so that the leading edge is no longer angled downwards. As Table 12 demonstrates, this very-low-drag design offers a 5.7% drag saving over the current generation of lightbars. The profile outlined in Figure 18 represents a highly optimised design that reduces lightbar self-drag by over 70% and further reduces vehicle roof and rear drag by 3.5 and 4.5 counts, respectively. For context, fitting this lightbar to a Hyundai Kona would increase unmarked vehicle drag by only 2.8%, which is only due to a frontal area increase, as the 0.313 C_D would be lower than that of the unmarked Kona (0.316). Therefore, this final design should form the basis of the next generation of low-drag lightbars for

emergency service vehicles, and fleet managers could consider highlighting its design as a requirement to suppliers when tendering for their next order of lightbars.



Figure 18. A rendered image of the final design of the low-drag lightbar.

Table 12. Drag reduction for the low-drag-lightbar final design over the baseline lightbar (Kona).

	C_D	C_D % Change	Area (m ²)	Area % Change	Drag Change
Hyundai Kona M	0.332	-	2.33961	-	-
Kona M-LDL Final Design	0.313	-5.7%	2.33978	0.0%	-5.7%

5. Conclusions

In conclusion, the current generation of lightbars used on emergency vehicles were studied to quantify their effects on fuel consumption and to find ways to improve their drag performance by using different modifications. Initial simulations on a range of vehicles found an 8–11% drag increase when fitting a lightbar to square-back vehicles. The drag penalty for mounting it on vehicles with rear-slanting roofs such as fastbacks and notchbacks would be higher, hence highlighting the suitability for square-back sedans and SUVs when mounting external lightbars. As the lightbar was shown to cause a relatively low drag increase, its effect on the driving range would not be overly detrimental and thus should not discourage the use of external lightbars on electric vehicles. For reference, the 10.3% drag increase reported for mounting the lightbar on an estateback police vehicle is equivalent to that resulting from driving a standard electric vehicle at 105 km/h instead of 100 km/h, emphasising the relatively low-drag nature of the current generation of lightbars. Additionally, the expected fuel consumption increase for five different police vehicles fitted with lightbars was estimated numerically to be between 3.53% and 4.41%, which is in excellent agreement with the 3.82% recorded from fuel economy data for 1650 police vehicles in April 2023.

A study into the effects of positioning found that lowering a detailed lightbar to its lowest position did not reduce drag compared with the standard height position. This was due to the lightbar’s mounting mechanism in its condensed form producing additional drag effects that offset any drag savings. When repeated on a simplified lightbar with a simplified mounting mechanism, a drag reduction was found for the lowest position. Raising the lightbar above the standard position was found to cause substantial drag increases of over 10%. Angling the lightbar was found to have a negligible effect on drag up to an angle of 2.5 degrees. At angles greater than this, the drag penalty was found to rise by approximately 4% for every additional 2.5 degrees. A study into the potential of fitting a drag-reducing ramp ahead of the lightbar was conducted. In all eight ramp designs, no appreciable drag reduction was realised, hence highlighting that fitting a ramp ahead of the current generation of lightbars would most likely increase drag. Noise production associated with the lightbar was found to be highest in the wake of the lightbar and, in some cases, reported an 8 dB increase in noise levels between the front and rear regions. Therefore, lowering lightbar noise would require the use of an appendable device to the rear of the lightbar that reduces the wake effects producing noise.

Finally, a study into the most optimal low-drag profile for the next generation of lightbars was conducted. The optimal lightbar design encourages overflow rather than underflow, combined with a tapered rear that does not excessively taper upwards, to bring the flow direction out of sync with the roof curvature. Appendable clip-on devices were designed based on the optimal lightbar for mounting on the current generation of lightbars. A simple rear clip-on was found to be most effective, reducing vehicle drag by

approximately 2.5%. The final optimised lightbar design increased unmarked vehicle drag by only 2.8%, which was a threefold improvement compared with the current generation of lightbars. Planned future work will include the on-road testing of police vehicles to further validate the results by using constant-speed tests to measure drag.

Author Contributions: Conceptualisation, M.G.C.; methodology, M.G.C.; software, M.J.O. and M.G.C.; validation, M.G.C.; formal analysis, M.G.C.; investigation, M.G.C.; resources, M.J.O. and A.I.; data curation, M.G.C.; writing—original draft preparation, M.G.C.; writing—review and editing, M.G.C.; visualisation, M.G.C.; supervision, M.J.O. and A.I.; project administration, M.J.O. and A.I.; funding acquisition, M.G.C., M.J.O. and A.I. All authors have read and agreed to the published version of the manuscript.

Funding: This research was funded by The Irish Research Council (grant number EPSPG/2022/213) and Science Foundation Ireland (grant number 22/NCF/EI/11277). The APC was funded by Science Foundation Ireland (grant number 22/NCF/EI/11277).

Data Availability Statement: The data presented in this study are available upon request from the corresponding author. The data are not publicly available due to the hosting costs for large datasets.

Acknowledgments: The support of UCD SONIC and ICHEC Kay for the use of their HPC resources.

Conflicts of Interest: The authors declare no conflicts of interest. The funders had no role in the design of the study; in the collection, analysis, or interpretation of data; or in the writing of the manuscript.

Abbreviations

The following abbreviations are used in this manuscript:

CFD	Computational Fluid Dynamics
RANS	Reynolds Averaged Navier–Stokes
LES	Large eddy simulation
SST	Shear Stress Transport
HPC	High-Performance Computing
EV	Electric vehicle
SBES	Stress-Blended Eddy Simulation
M	Marked (lightbar fitted)
SL	Simplified lightbar
DRR	Drag-reducing ramp
LDL	Low-drag lightbar

References

1. EEA. Transport and Mobility. 2023. Available online: <https://www.eea.europa.eu/en/topics/in-depth/transport-and-mobility> (accessed on 4 April 2024).
2. Stoica, T.L. Roof-Mounted Light Systems on Police Vehicles. 1982. Number: HS-033 051. Available online: <https://www.ojp.gov/njrs/virtual-library/abstracts/roof-mounted-light-systems-police-vehicles> (accessed on 4 April 2024).
3. Raub, R.A. Removal of Roof-Mounted Emergency Lighting from Police Patrol Vehicles: An Evaluation. In *Transportation Research Record*; Transportation Research Board: Washington, DC, USA, 1985; ISBN 9780309039635.
4. Hansen, J.H.; Blankenship, J.L. Highway Patrol Light Bar Effects on Vehicle Fuel Efficiency. In *Proceedings of the Transportation Research Record*, Washington, DC, USA, 13–16 January 1986; Volume 1059.
5. Chowdhury, H.; Alam, F.; Khan, I.; Djamovski, V.; Watkins, S. Impact of Vehicle add-ons on Energy Consumption and Greenhouse Gas Emissions. *Procedia Eng.* **2012**, *49*, 294–302. [[CrossRef](#)]
6. Taherkhani, A.R.; Gilkeson, C.; Gaskell, P.; Hewson, R.; Toropov, V.; Rezaienia, A.; Thompson, H. Aerodynamic CFD Based Optimization of Police Car Using Bezier Curves. *SAE Int. J. Mater. Manuf.* **2017**, *10*, 85–93. [[CrossRef](#)]
7. Taherkhani, A.R.; de Boer, G.N.; Gaskell, P.H.; Gilkeson, C.A.; Hewson, R.W.; Keech, A.; Thompson, H.M.; Toropov, V.V. Aerodynamic Drag Reduction of Emergency Response Vehicles. *Adv. Automob. Eng.* **2015**, *4*. [[CrossRef](#)]
8. Iozsa, D.; Ilea, L.; Fratila, G. Influence of warning lights for intervention vehicles on aerodynamic performance. *IOP Conf. Ser. Mater. Sci. Eng.* **2020**, *997*, 012118. [[CrossRef](#)]
9. Connolly, M.G.; O'Rourke, M.J.; Ivankovic, A. A Drag Reduction Study on the Aerodynamics of the Irish Taxi Sign. *Fluids* **2023**, *8*, 238. [[CrossRef](#)]
10. Chen, Y.; Meier, A. Fuel consumption impacts of auto roof racks. *Energy Policy* **2016**, *92*, 325–333. [[CrossRef](#)]
11. Zacharof, N.G.; Fontaras, G.; Ciuffo, B.; Tsiakmakis, S.; Anagnostopoulos, K.; Marotta, A.; Pavlovic, J. *Review of in Use Factors Affecting the Fuel Consumption and CO₂ Emissions of Passenger Cars*; Publications Office of the European Union: Luxembourg, 2016.

12. Sun, B. Revisiting the Reynolds-averaged Navier–Stokes equations. *Open Phys.* **2021**, *19*, 853–862. [[CrossRef](#)]
13. Menter, F. *Zonal Two Equation kw Turbulence Models for Aerodynamic Flows*; American Institute of Aeronautics and Astronautics: Reston, VA, USA, 1993. [[CrossRef](#)]
14. Zhang, C.; Bounds, C.P.; Foster, L.; Uddin, M. Turbulence Modeling Effects on the CFD Predictions of Flow over a Detailed Full-Scale Sedan Vehicle. *Fluids* **2019**, *4*, 148. [[CrossRef](#)]
15. Aultman, M.; Wang, Z.; Auza-Gutierrez, R.; Duan, L. Evaluation of CFD methodologies for prediction of flows around simplified and complex automotive models. *Comput. Fluids* **2022**, *236*, 105297. [[CrossRef](#)]
16. Menter, F. Stress-Blended Eddy Simulation (SBES)—A New Paradigm in Hybrid RANS-LES Modeling. In *Progress in Hybrid RANS-LES Modelling*; Notes on Numerical Fluid Mechanics and Multidisciplinary Design; Hoarau, Y., Peng, S.H., Schwamborn, D., Revell, A., Eds.; Springer: Cham, Switzerland, 2018; pp. 27–37. [[CrossRef](#)]
17. Schuetz, T.C. *Aerodynamics of Road Vehicles*; SAE International: Warrendale, PA, USA, 2015.
18. Lighthill, M.J. On sound generated aerodynamically I. General theory. *Proc. R. Soc. Lond. Ser. A Math. Phys. Sci.* **1952**, *211*, 564–587.
19. Williams, J.E.F.; Hawkings, D.L. Sound Generation by Turbulence and Surfaces in Arbitrary Motion. *Philos. Trans. R. Soc. Lond. Ser. A Math. Phys. Sci.* **1969**, *264*, 321–342. [[CrossRef](#)]
20. Connolly, M.G.; O'Rourke, M.J.; Ivankovic, A. Reducing Aerodynamic Drag on Flatbed Trailers for Passenger Vehicles Using Novel Appendable Devices. *Fluids* **2023**, *8*, 289. [[CrossRef](#)]
21. Zore, K.; Caridi, D. *Automotive Aerodynamic Noise Prediction Using Scale Resolved Stress-Blended Eddy Simulation*; Institute of Noise Control Engineering: Washington, DC, USA, 2020; Volume 262, pp. 350–362.
22. Ekman, P.; Larsson, T.; Virdung, T.; Karlsson, M. *Accuracy and Speed for Scale-Resolving Simulations of the DriveAer Reference Model*; SAE International: Warrendale, PA, USA, 2019. [[CrossRef](#)]
23. Chow, K. Improving vehicle rolling resistance and aerodynamics. In *Alternative Fuels and Advanced Vehicle Technologies for Improved Environmental Performance*; Elsevier: Amsterdam, The Netherlands, 2022; pp. 459–481. [[CrossRef](#)]
24. A.R.C. The Effect of Aerodynamic Drag on Fuel Economy | ARC. Available online: <http://www.arcindy.com/effect-of-aerodynamic-drag-on-fuel-economy.html> (accessed on 4 April 2024).
25. Ekman, P.; Gardhagen, R.; Virdung, T.; Karlsson, M. *Aerodynamic Drag Reduction of a Light Truck—From Conceptual Design to Full Scale Road Tests*; SAE International: Warrendale, PA, USA, 2016. [[CrossRef](#)]
26. Viswanathan, H.; Chode, K.K. The Role of Forebody Topology on Aerodynamics and Aeroacoustics Characteristics of Squareback Vehicles using Computational Aeroacoustics (CAA). *Flow Turbul. Combust.* **2024**, *112*, 1055–1081. [[CrossRef](#)]
27. Nusser, K. Investigation of the Fluid-Structure-Acoustics Interaction on a Simplified Car Model. Ph.D. Thesis, Friedrich-Alexander-Universität Erlangen-Nürnberg, Erlangen, Germany, 2019.
28. Nusser, K.; Becker, S. Numerical investigation of the fluid structure acoustics interaction on a simplified car model. *Acta Acust.* **2021**, *5*, 22. [[CrossRef](#)]
29. Binning, E. Arresting Image Update to Save Police Force \$800,000. 2008. Available online: <https://www.nzherald.co.nz/nz/arresting-image-update-to-save-police-force-800000/U6KNMQDJEIMTL3NSG77ULJ4FHM/> (accessed on 4 April 2024).

Disclaimer/Publisher's Note: The statements, opinions and data contained in all publications are solely those of the individual author(s) and contributor(s) and not of MDPI and/or the editor(s). MDPI and/or the editor(s) disclaim responsibility for any injury to people or property resulting from any ideas, methods, instructions or products referred to in the content.